Fe-Substituted Mullite Powders for the In Situ Synthesis of Carbon Nanotubes by Catalytic Chemical Vapor Deposition

Valdirene G. de Resende,[†,‡] Xu Hui,[‡,§] Christophe Laurent,[‡] Alicia Weibel,[‡] Eddy De Grave,[†] and Alain Peigney*[,‡]

Department of Subatomic and Radiation Physics, University of Ghent, B-9000 Gent, Belgium, and Université de Toulouse, Institut Carnot CIRIMAT, CNRS-UPS, Université Paul-Sabatier, Bât. 2R1, 118 Route de Narbonne, 31062 Toulouse Cedex 9, France

Powders of iron-substituted mullite were prepared by combustion and further calcination in air at different temperatures. A detailed study involving notably Mössbauer spectroscopy showed that the Fe^{3+} ions are distributed between the mullite phase and a corundum phase that progressively dissolves into mullite upon the increase in calcination temperature. Carbon nanotube−Fe−mullite nanocomposites were prepared for the first time by a direct method involving a reduction of these powders in H_2-CH_4 and without any mechanical mixing step. The carbon nanotubes formed by the catalytic decomposition of CH_4 on the smallest metal particles are mostly double-walled and multiwalled, although some carbon nanofibers are also observed.

1. Introduction

Ceramic-matrix nanocomposites are one of the many applications of carbon nanotubes.[1] One of the main hurdles for the successful preparation of such composites is to obtain a homogeneous distribution of undamaged carbon nanotubes into the matrix. To obviate a mechanical-mixing step during the preparation of the composite powder, a direct method for the *in situ* synthesis of the carbon nanotubes into an Al_2O_3 matrix has been proposed.[2] It is based on a catalytic chemical vapor deposition route involving the reduction in H_2-CH_4 gas atmosphere of $Al_2O_3-Fe_2O_3$ solid solutions, producing carbon nanotube−Fe-Al_2O_3 nanocomposite powders. The reduction first produces nanometric Fe particles that are active for the decomposition of CH_4 and, subsequently, for the formation of carbon nanotubes, notably single- and double-walled carbon nanotubes if their diameter is small enough (<ca. 5 nm).[3,4] This method was subsequently expanded to powders with $MgAl_2O_4$-,[5] MgO-,[6] and ZrO_2-[7] matrixes.

^{57}Fe Mössbauer spectroscopy offers several advantages for studies of iron-containing compounds. The spectra, and parameters derived from these, are very sensitive to the electronic, magnetic, and structural characteristics of the probed material, and as such, Mössbauer spectroscopy is a useful tool for phase identification and quantification of mixtures of Fe-bearing materials. Although iron species are often involved in carbon nanotube formation processes, only relatively few carbon nanotube-related studies, apart from those by some of the present authors,[4,8−19] report on Mössbauer data with regard to the formation, evolution, and the spatial distribution of Fe-containing particles after synthesis of the carbon nanotubes by catalytic chemical vapor deposition methods.[20−24]

Mullite is the name of some $Al_2O_3-SiO_2$ compounds. The most widely studied form is $Al_6Si_2O_{13}$ (also commonly designated $3Al_2O_3{:}2SiO_2$), but considerable variations in crystal structure and chemical composition have been found.[25−30] This material is increasingly important for electronic, optical, and high-temperature structural applications, which, however, are limited by a low toughness. However, carbon nanotube−mullite nanocomposites are seldom studied. Wang et al.[31] prepared such materials by mixing powders of carbon nanotubes, Al_2O_3, and SiO_2.

In the present work, the authors for the first time have studied the formation of carbon nanotubes from Fe-substituted mullite powders. These catalytic materials and the carbon nanotube−Fe-mullite composite powders will be studied by several techniques including electron microscopy and Mössbauer spectroscopy.

2. Experimental Section

2.1. Synthesis of the Fe-Substituted Mullite Powders. A combustion method similar to the one reported for the synthesis of pure mullite[32−34] was used in order to prepare 6 g of $Fe_{0.6}Al_{5.4}Si_2O_{13}$ powder. The required proportions of $Al(NO_3)_3\cdot 9H_2O$ (27.41 g), $Fe(NO_3)_3\cdot 9H_2O$ (3.28 g), and NH_4NO_3 (5/6 of the molar quantity of the metal nitrates, i.e. 5.41 g) were dissolved in an aqueous suspension of colloidal SiO_2 (1.62 g), using the minimum amount of water. The required proportion of urea (the fuel) was added under continuous stirring up to complete dissolution. The urea proportion (24.36 g) was twice the so-called stoichiometric ratio calculated from the total oxidizing valence of the nitrates and the reducing valence of urea.[35] The dish containing the mixture was placed in a furnace preheated at 600 °C, keeping the door of the furnace open. After water evaporation, a combustion reaction takes place between the nitrates and urea, thus producing an oxide powder. The as-prepared powder was divided into several batches, which were calcined in air at different temperatures in the range 800−1400 °C (heating rate to the desired temperature equal to 300 °C/h, 1 h at the desired temperature, natural cooling down to room temperature). The powders are hereafter code-named as C800,..., C1400.

2.2. Synthesis of the Carbon Nanotubes. The carbon nanotube−Fe−mullite nanocomposite powders were prepared

To whom correspondence should be addressed. Fax: +33 561 55 61 63. E-mail: peigney@chimie.ups-tlse.fr.

[†] University of Ghent.

[‡] Université Paul-Sabatier.

[§] On temporary leave from the College of Petrochemical Technology, Lanzhou University of Technology, Lanzhou, Gansu Province, P.R. China.

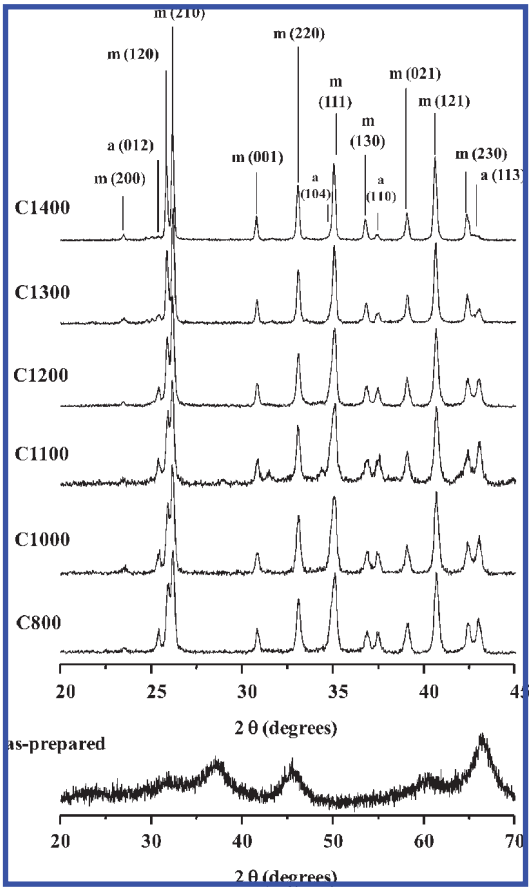

Figure 1. X-ray diffraction patterns at 295 K of the as-prepared powder and after calcination in air at different temperatures: m, mullite; a, corundum. Note that the 2θ range shown is not the same for the as-prepared powders and the other ones.

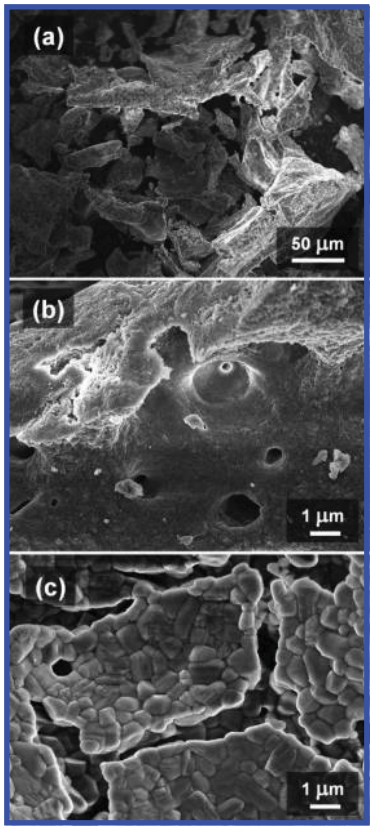

Figure 2. Field-emission-gun scanning electron microscopy images of selected powders: C1100 (a); C1200 (b); C1400 (c).

by a catalytic chemical vapor deposition treatment in H_2-CH_4 (20 mol % CH_4, maximum temperature 1050 °C, no dwell, heating, and cooling rates 300 °C/h). The flowing gas was dried on P_2O_5, and its composition was monitored by mass-flow controllers. The so-obtained powders are named as C800R,..., C1400R.

2.3. Characterization. X-ray diffraction patterns were recorded using a Bruker D4 Endeavor diffractrometer equipped with a Cu Kα radiation tube. The carbon content in the nanocomposite powders was measured by the flash combustion method with an accuracy of ±2%. The specific surface area of the powders was measured by the BET method (Micrometrics Flow Sorb II 2300) using nitrogen adsorption at liquid nitrogen temperature. Mössbauer spectra at 295 and 80 K were collected. A spectrometer operating in constant acceleration mode with triangular reference signal and with ^{57}Co (Rh) source was used. Accumulation of data was made in 1024 channels. The spectrometer has been calibrated by collecting at 295 K the spectrum of a standard hematite (α-Fe_2O_3) or a standard metallic iron foil. The isomer shifts quoted hereafter are referenced with respect to α-Fe at room temperature. The powders were observed by field-emission-gun scanning electron microscopy (JEOL JSM 6700F). The powders were also observed by high-resolution transmission electron microscopy (Jeol JEM 2100F).

3. Results and Discussion

3.1. Fe-Substituted Mullite Powders. X-ray diffraction pattern (Figure 1) analysis of the as-prepared powder reveals wide peaks characteristic of a poorly crystallized transition alumina. No mullite or iron oxide peaks are detected. According to Burgos-Montes et al.,[34] using NH_4NO_3 as a combustion aid should have allowed for the preparation of crystallized mullite. The difference may be due to the present use of an open furnace, resulting in a less uniform heating, as opposed to a purpose-build reaction device as described by these authors.[34] Peaks characteristic of mullite and peaks accounting for α-Al_2O_3 (corundum) are detected for all calcined powders (Figure 1). The shift of some peaks from one powder to another may reflect that the corresponding phases contain different amounts of iron. The intensity of the corundum peaks appears to be quite constant for C800−C1100 and regularly decreases for C1200−C1400, possibly revealing its progressive dissolution into the mullite upon the increase in calcination temperature. The mullite peaks become narrower upon the increase in calcination temperature, reflecting crystallite growth. The specific surface area of the C800−C1200 powders is in the range 1.5−4.4 m^2/g and is still lower for C1300 (1.0 m^2/g) and C1400 (0.5 m^2/g). These values are considerably lower than those reported by authors using a very similar method,[33,34] although the reason for this is not clear. The field-emission-gun scanning electron microscopy image of a typical powder (C1100) shows grains several tens of micrometers in size and fairly irregular in shape (Figure 2a). It was not possible to distinguish the mullite from the corundum particles on such images. Higher magnification images of such grains reveal that they are quite porous and made-up of submicrometric crystallites, as shown on a typical image for C1200 (Figure 2b), except for C1400 (Figure 2c) where the crystallites are micrometric, because of the higher calcination temperature.

Mössbauer spectra were recorded at 295 and 80 K for all calcined powders. In order to check for a possible presence of small amounts of hematite (α-Fe_2O_3) in the samples, three of

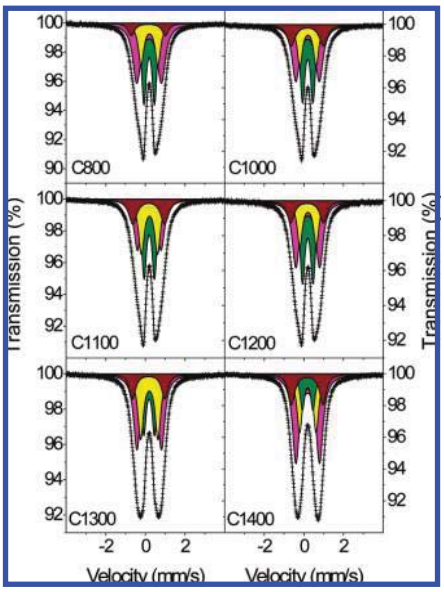

Figure 3. Mössbauer spectra at 295 K of the calcined powders. Fe^{3+}/Al_2O_3 (olive); Fe^{3+}/mullite: site A (magenta), site B (yellow), and site C (brown).

these were selected and their Mössbauer spectra (not shown) collected over a broad velocity scale (±11 mm/s). The sextet characteristic of hematite was not observed, nor any other sextet component. Consequently, hematite had not been formed in the calcination process, at least not to measurable abundance (about 2%), in agreement with the X-ray diffraction results. Thus, in a next stage the 295 K Mössbauer spectra for all powders were acquired over a narrow velocity scale (±4 mm/s), implying a higher resolution (Figure 3). All Mössbauer spectra are characterized by a broad, slightly asymmetric, doublet shape, which might be explained by the presence of more than one discrete component. This contrasts with earlier studies for Fe-substituted mullite[36,37] where only a single quadrupole doublet with Mössbauer parameters claimed to be typical for octahedrally coordinated Fe^{3+} was used for the fit. However, the structure of mullite is made up of chains of edge-sharing AlO_6 octahedra running parallel to the crystallographic *c*-axis and cross-linked by AlO_4 and SiO_4 tetrahedra occurring in dimers and trimers. The octahedral site bears 66% of the total Al^{3+} ions. The first tetrahedral site contains both Al^{3+} (25% of total) and Si^{4+}. The third site is a distorted tetrahedron occupied by 9% of the total Al^{3+} ions. Thus, any of these three sites may be partly substituted by Fe^{3+}. Indeed, several authors proposed a deconvolution of the Mössbauer spectrum into three doublets: Cardile et al.[38] and Parmentier et al.[39] found one octahedral and two tetrahedral sites, whereas Mack et al.[40] proposed two octahedral and one tetrahedral sites. A three-doublet model indeed produced excellent reproductions of the present Mössbauer spectra with no significant mismatches. However, unacceptable inconsistencies in the calculated area fractions of the three components were obvious. A fourth doublet, accounting for Fe^{3+} ions in the α-alumina (corundum) phase, consistent with the identification of this phase in the X-ray diffraction patterns, was therefore included in the fitting model. No restrictions had to be imposed for the iteration procedure to reach convergency with reasonable parameter values. The adjusted hyperfine parameter values are listed in Table 1. The goodness-of-fit χ^2 was on the average found to be around 1.1. The Fe^{3+}/corundum doublet has hyperfine parameters ($\Delta E_Q \approx 0.53$ mm/s and $\delta \approx 0.29$ mm/s at 295 K) that are very close to those found earlier for Fe^{3+} ions in the corundum lattice.[4,41] The ΔE_Q values of the three Fe^{3+}/mullite doublets are broadly in line with those reported[38−40] for Fe-substituted mullites. As noted by Parmentier et al.,[39] differences concerning the distribution of the Fe^{3+} ions among the lattice sites may be attributed to different synthesis routes and thermal treatments. The adjusted values of δ, ΔE_Q, and Γ for the four doublets are not significantly affected by the calcination temperature. Interestingly, the area fraction (RA) of the Fe^{3+}/corundum doublet is more or less constant (∼ 30%) from C800 to C1200 but gradually decreases for C1300 (21%) and C1400 (12%). This finding corroborates the qualitative results of the above X-ray diffraction analyses showing the progressive dissolution of the Fe-substituted alumina into the Fe-substituted mullite. Although the Mössbauer spectra reveal the presence of three distinct Fe^{3+} sites for the mullite phase, the precise nature of the coordination of these respective sites cannot be inferred straightforwardly on the basis of the numerical results. According to the extensive survey of Menil,[42] room temperature isomer-shift values for Fe^{3+} are found within the ranges 0.10−0.30 mm/s and 0.28−0.50 mm/s for tetrahedral and octahedral sites, respectively. The present δ values, being equal for all three lattice sites within the estimated error limits of ±0.02 mm/s, are very close to the bordering value between the two types of coordination. Consequently, site assignment exclusively based on the δ value is not possible in the present case. As mentioned above, one of the tetrahedral sites is highly distorted. It is therefore tempting to attribute the doublet with the highest quadrupole splitting (∼1.6−1.7 mm/s; site C in Table 1) to this site. The relatively large iron−oxygen bond lengths would then explain the relatively high isomer shift values observed for this doublet. Further, it is proposed that none of the two other doublets having smaller quadrupole splittings (site A and site B in Table 1) is due to Fe^{3+} in tetrahedral sites, because one would expect to measure a significantly lower isomer shift than the value obtained for the C sites. Therefore, in agreement with Mack et al.,[40] it is suggested that site A and site B both exhibit 6-fold coordination. The different values for the respective quadrupole splittings cannot be inferred from the present measurements.

3.2. Carbon Nanotube-Fe-Mullite Composite Powders. The X-ray diffraction patterns of the nanocomposite powders are shown in Figure 4. Mullite and corundum peaks are detected as in the parent oxide powders. Interestingly, α-Fe and hercynite ($FeAl_2O_4$) are detected as well. The intensity of the (110) α-Fe peak is strong for C800R-C1100R and lower for C1200R and C1300R, and the peak is not detected for C1400R. It seems that the intensity of the (311) hercynite peak decreases slightly upon the increase of the calcination temperature. Fe_3C (cementite) may also be present in some powders, but it is difficult to clearly separate the patterns of α-Fe and Fe_3C because the respective main diffraction peaks are strongly overlapping. Note that two peaks (labeled U1 and U2 in Figure 4) detected for some powders could not be assigned to any specific phase. Interestingly, it seems that the evolution of the intensity of these peaks more or less follows that for the (110) α-Fe peak.

The carbon content is constant (2.2 wt %) from C800R to C1200R but gradually decreases for C1300R (0.3 wt %) and C1400R (0.1 wt %). The specific surface area is higher for C800R, C1000R, C1100R, and C1200R (3.9, 6.1, 6.2, and 5.5 m^2/g, respectively) than for C1300R (1.4 m^2/g) and C1400R (0.7 m^2/g). These values tend to be slightly higher than those found for the corresponding catalytic materials. As pointed out earlier,[2,8] it is the deposition of carbon in the composite powder, particularly in the form of carbon nanotubes, which is responsible for most of this supplementary surface area.

TABLE 1: Mössbauer Hyperfine Parameters at 295 and 80 K of the Powders Prepared by Combustion and Further Calcination in Air[a]

	Fe^{3+} in alumina				Fe^{3+} in mullite											
					site A				site B				site C			
	δ (mm/s)	ΔE_Q (mm/s)	RA (%)	Γ (mm/s)	δ (mm/s)	ΔE_Q (mm/s)	RA (%)	Γ (mm/s)	δ (mm/s)	ΔE_Q (mm/s)	RA (%)	Γ (mm/s)	δ (mm/s)	ΔE_Q (mm/s)	RA (%)	Γ (mm/s)
295 K																
C800	0.31	0.53	32	0.29	0.30	1.24	41	0.49	0.32	0.85	20	0.33	0.26	1.72	7	0.40
C1000	0.30	0.53	30	0.29	0.30	1.18	36	0.46	0.32	0.82	19	0.32	0.28	1.62	15	0.49
C1100	0.31	0.52	29	0.29	0.31	1.18	29	0.43	0.32	0.81	26	0.36	0.28	1.60	16	0.49
C1200	0.31	0.53	31	0.30	0.31	1.20	37	0.44	0.32	0.83	19	0.32	0.27	1.65	13	0.43
C1300	0.30	0.54	21	0.28	0.31	1.23	39	0.41	0.31	0.87	28	0.35	0.28	1.63	12	0.40
C1400	0.30	0.54	12	0.27	0.31	1.19	48	0.42	0.31	0.84	24	0.33	0.28	1.59	16	0.41
80 K																
C800	0.41	0.54	33	0.32	0.40	1.28	38	0.50	0.42	0.88	22	0.35	0.37	1.75	7	0.40
C1000	0.41	0.52	30	0.31	0.41	1.21	35	0.47	0.42	0.83	20	0.32	0.39	1.65	15	0.50
C1100	0.41	0.51	27	0.30	0.41	1.23	29	0.44	0.42	0.82	29	0.35	0.39	1.65	15	0.51
C1200	0.41	0.54	31	0.31	0.41	1.23	37	0.46	0.42	0.86	19	0.31	0.37	1.64	13	0.49
C1300	0.41	0.52	21	0.30	0.41	1.25	39	0.42	0.42	0.87	28	0.34	0.37	1.65	12	0.40
C1400	0.41	0.51	12	0.29	0.41	1.19	48	0.43	0.41	0.82	24	0.34	0.37	1.61	16	0.41

[a] ΔE_Q, quadrupole splitting; δ, isomer shifts; Γ, line width; RA, relative spectral areas. The values of isomer shifts are with reference to metallic iron. The estimated errors in the quadrupole splittings and isomer shifts are 0.02 and 0.01 mm/s, respectively. For the relative spectral areas, the error is about 4% of the actual values, and for the line width, it is 0.02 mm/s.

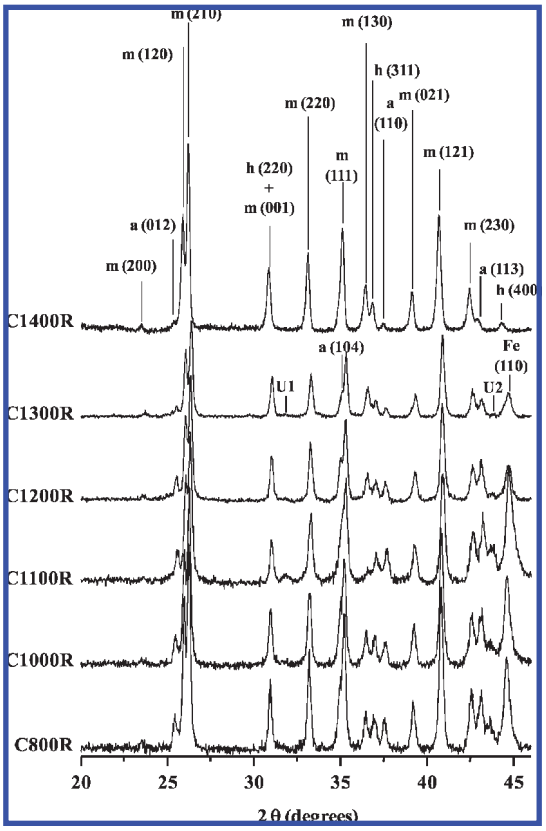

Figure 4. X-ray diffraction patterns at 295 K of the carbon nanotube−Fe−mullite nanocomposite powders: m, mullite; a, corundum; h, hercynite; Fe, α-Fe. U1 and U2: unidentified peaks.

Typical field-emission-gun scanning electron microscopy images are shown in Figures 5 and 6. For all powders, long, flexible filaments are observed on the surface of the oxide grains (Figure 5c, e, f, and j). These filaments show a smooth and regular surface, have a diameter smaller than 30 nm, and a length of the order of a few tens of micrometers (Figure 5d and i). From earlier results, it is known that such filaments are isolated carbon nanotubes and/or carbon nanotube bundles. The presence of undesirable carbon species, together with carbon nanotubes,

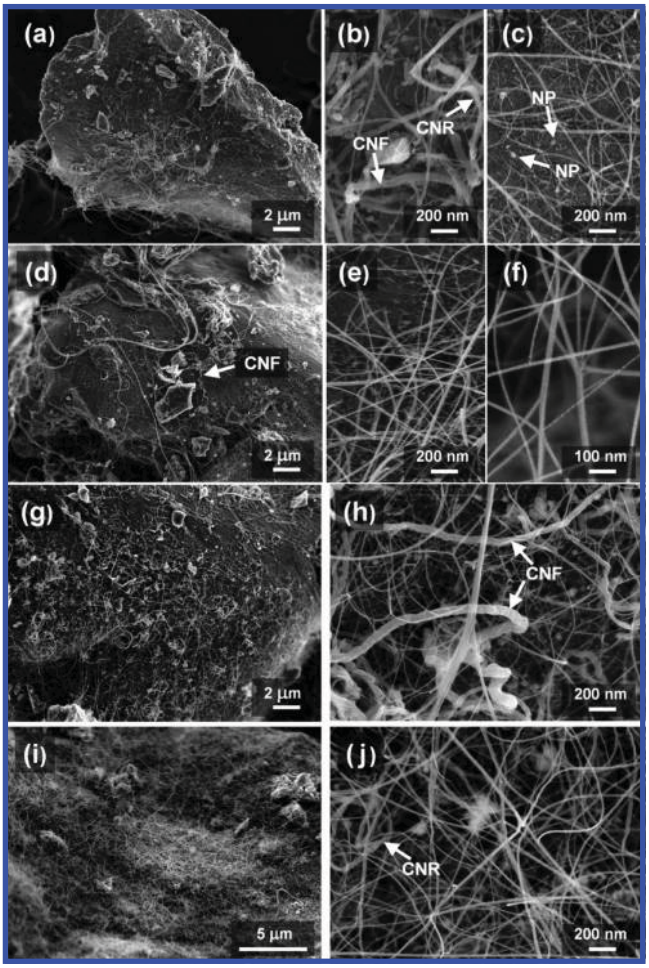

Figure 5. Field-emission-gun scanning electron microscopy images of the carbon nanotube−Fe−mullite nanocomposite powders: C800R (a−c); C1000R (d−f); C1100R (g−j). NP, Fe or Fe_3C nanoparticle; CNF, carbon nanofiber; CNR, carbon nanoribbon.

is also observed in some areas of all the powders. The most frequently observed species are carbon nanofibers (Figure 5b, d, and h), easily detectable by their rough surface and their

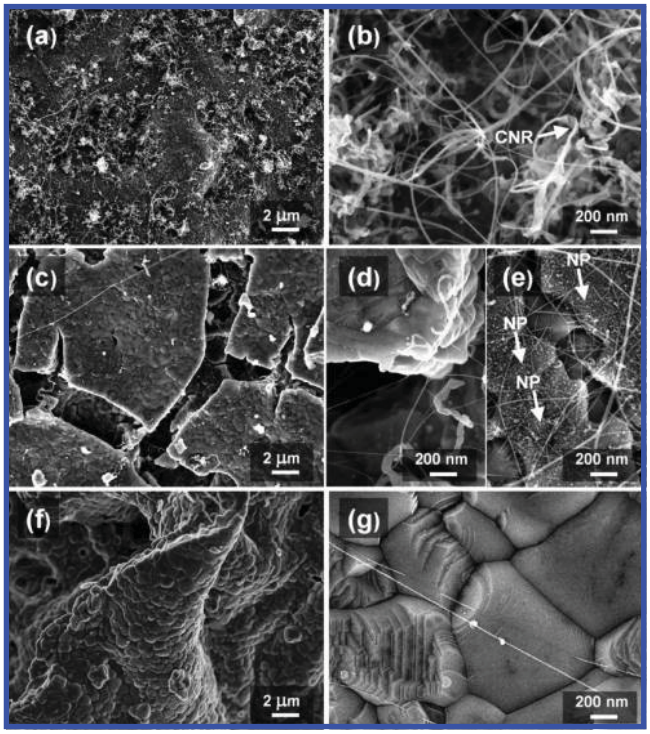

Figure 6. Field-emission-gun scanning electron microscopy images of the carbon nanotube−Fe−mullite nanocomposite powders: C1200R (a, b); C1300R (c−e); C1400R (f, g).

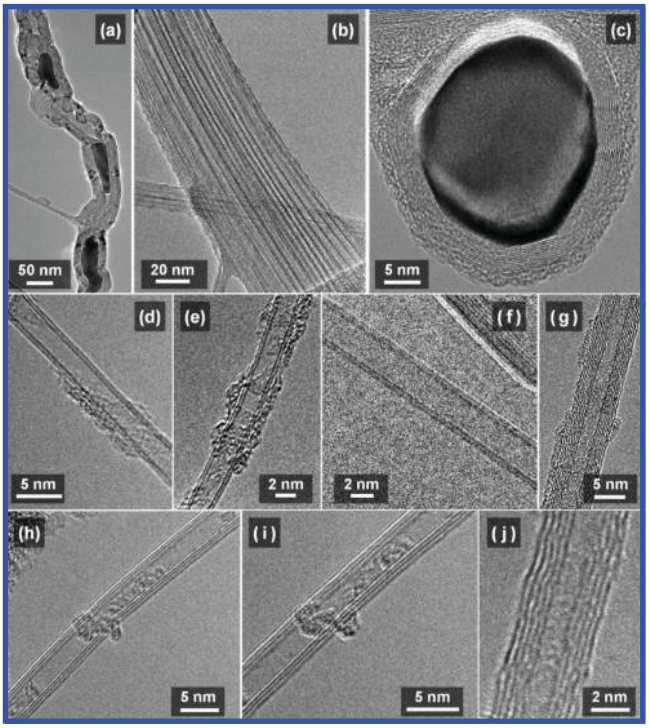

Figure 7. Typical high-resolution transmission electron microscopy images showing a carbon nanofiber (a), a carbon nanotubes bundle (b), a Fe or Fe_3C particle covered by graphene layers (c), double-walled carbon nanotubes (d−f), and multiwalled carbon nanotubes (g−j).

diameter in the range 30−80 nm. Some carbon nanoribbons, 50−100 nm in width (Figure 5b, j, Figure 6b) are rarely observed. Fe or Fe_3C spherical nanoparticles, with a diameter in the range 5−20 nm, are also observed on the surface of some oxide grains, particularly when the grains are not completely covered by a thick layer of carbon filaments (Figure 5c, Figure 6e). Significantly less carbon nanotubes are observed for powders C1300R (Figure 6c−e) and C1400R (Figure 6f and g), in agreement with their much lower carbon content (0.3 and 0.1 wt %, respectively) compared to those of the other powders (2.2 wt %). For the powders C800R, C1000R, and C1100R, some grains are homogeneously covered by a network of carbon nanotubes, without any carbon nanofibers or carbon nanoribbons (Figure 5c, e, f, i, and j) but other areas or grains are covered by a mixture of carbon nanotubes, carbon nanofibers, and a few carbon nanoribbons (Figure 5a, b, d, g, and h). A similar mixture is observed for C1200R (Figure 6a and b). For C1300R, rare grains covered by carbon nanotubes and numerous nanoparticles are observed (Figure 6e).

Typical high-resolution transmission electron microscopy images show the different carbon species, including a carbon nanofiber (Figure 7a), a carbon nanotubes bundle (Figure 7b), a Fe or Fe_3C particle covered by graphene layers (Figure 7c), double-walled carbon nanotubes (Figure 7d−f), and multiwalled carbon nanotubes (Figure 7g−j). Disordered carbon is observed at the surface of some carbon nanotubes, but a fair proportion of it was formed during the observation because the carbon nanotubes, notably the thinner ones, were damaged by the electron beam.

The Mössbauer spectra at 80 K of the reduced powders are shown in Figure 8, and the corresponding Mössbauer parameters are summarized in Table 2. All spectra have been analyzed using Lorentzian line shapes. In general, eight components were found to be required to obtain adequate fits: (i) an outer sextet showing hyperfine parameters that are characteristic of α-Fe, (ii) an inner

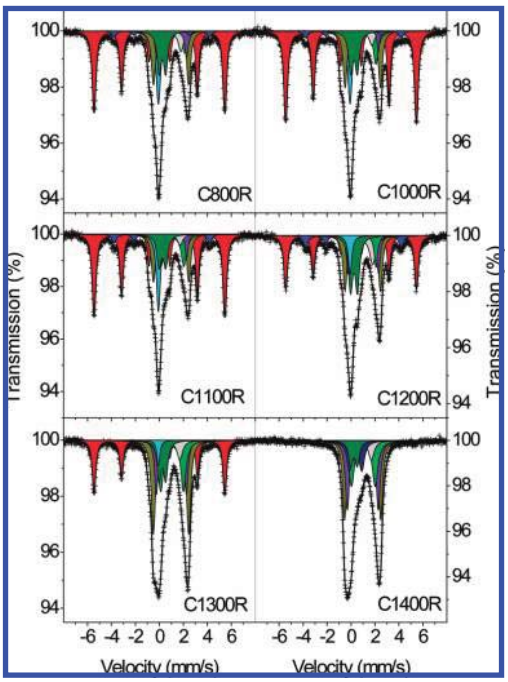

Figure 8. Mössbauer spectra at 80 K of the carbon nanotube−Fe−mullite nanocomposite powders. Fe^{3+}/Al_2O_3 (olive); α-Fe (red); Fe_3C (blue); γ-Fe-C (cyan); Fe^{2+}/hercynite (dark yellow, violet, green, light gray); Fe^{3+}/hercynite (navy).

sextet that was fitted with parameters of Fe_3C, (iii) a singlet that corresponds to a γ-Fe phase, possibly alloyed with carbon (γ-Fe-C), (iv) an Fe^{3+} doublet due to iron ions in the lattice of corundum, and (v−viii) four Fe^{2+} doublets that were assigned to ferrous iron in tetrahedral and octahedral sites of hercynite. The goodness-of-fit χ^2 was on the average ∼1.07. Additionally, a ninth Fe^{3+} doublet was needed to be included in the fit of the

TABLE 2: Mössbauer Hyperfine Parameters at 80 K of Carbon Nanotube−Fe−Mullite Nanocomposite Powders[a]

	α-Fe				Fe_3C				Fe^{3+} in alumina				γ-Fe-C		
	B_{hf} (T)	δ (mm/s)	RA (%)	Γ (mm/s)	B_{hf} (T)	δ (mm/s)	RA (%)	Γ (mm/s)	δ (mm/s)	ΔE_Q (mm/s)	RA (%)	Γ (mm/s)	δ (mm/s)	RA (%)	Γ (mm/s)
C800R	33.9	0.11	40	0.32	24.7[b]	0.31[b]	4	0.35[b]	0.36	0.55	11	0.42	0.03	11	0.45
C1000R	33.9	0.11	42	0.32	24.7[b]	0.31[b]	4	0.35[b]	0.36[b]	0.55[b]	11	0.43	0.03[b]	10	0.44
C1100R	33.9	0.11	41	0.31	24.7[b]	0.31[b]	6	0.35[b]	0.36[b]	0.55[b]	9	0.43	0.03[b]	11	0.40
C1200R	33.9	0.11	28	0.35	24.7[b]	0.31[b]	7	0.35[b]	0.36	0.57	16	0.42	0.03	5	0.35
C1300R	33.8	0.11	24	0.34					0.36[b]	0.55[b]	11	0.40	0.03[b]	3	0.42
C1400R[c]									0.36[b]	0.55[b]	8	0.42			

	Fe^{2+} in Hercynite															
	tetrahedral site				tetrahedral site				octahedral site				octahedral site			
	δ	ΔE_Q (mm/s)	RA (%)	Γ (mm/s)	δ (mm/s)	ΔE_Q (mm/s)	RA (%)	Γ (mm/s)	δ (mm/s)	ΔE_Q (mm/s)	RA (%)	Γ (mm/s)	δ	ΔE_Q (mm/s)	RA (%)	Γ (mm/s)
C800R	1.09	2.94	15	0.40	1.13	2.49	6	0.35	1.07	1.67	7	0.52	1.23	1.92	6	0.39
C1000R	1.09	2.94	14	0.39	1.13	2.53	3	0.23	1.05	1.60	5	0.53	1.20	1.96	11	0.50
C1100R	1.09	2.96	13	0.39	1.13	2.53	4	0.27	1.03	1.62	4	0.54	1.20	1.91	12	0.53
C1200R	1.09	2.96	16	0.39	1.13	2.56	9	0.32	1.11	1.64	12	0.60	1.20	1.97	7	0.33
C1300R	1.08	2.95	25	0.40	1.11	2.52	13	0.35	1.04	1.55	7	0.55	1.17	1.90	17	0.52
C1400R[c]	1.08	3.00	26	0.39	1.09	2.58	23	0.41	1.08	1.45	9	0.54	1.14	1.98	21	0.56

[a] B_{hf}, hyperfine field; ΔE_Q, quadrupole splitting; δ, isomer shift; Γ, line width; RA, relative spectral area. The values of isomer shifts are with reference to metallic iron. Estimated errors in the quadrupole splittings and isomer shifts are 0.02 and 0.01 mm/s, respectively. For the relative spectral areas, the error is about 4% of the actual values, hyperfine field is 0.2 T, and line width is 0.02 mm/s. [b] Fixed parameters. [c] In that sample an extra Fe^{3+} doublet is present: $\delta \sim 0.49$ mm/s; $\Delta E_Q \sim 1.03$ mm/s; $\Gamma \sim 0.52$ mm/s; RA ~13%.

spectrum of sample C1400R. Its quadrupole splitting was found to be approximately 1.03 mm/s and isomer shift ~0.49 mm/s. This Fe^{3+} doublet could also be due to hercynite. Indeed, Larsson et al.[43] obtained a spectrum, of a very disordered sample, that was fitted using four Fe^{2+} doublets and one Fe^{3+} doublet which had hyperfine parameters ($\Delta E_Q \sim 0.95$ mm/s and $\delta \sim 0.47$ mm/s) very similar to the ones found in this work. Interestingly, no contribution for Fe^{3+}/mullite was detected. The RA values corresponding to the Fe^{3+}/corundum were found in the range 8−16%. The total contribution for hercynite is similar (33−34%) for C800R, C1000R, and C1100R. An increase is observed for C1200R (44%), C1300R (62%), and C1400R (92%). The α-Fe contribution in the Mössbauer spectra is similar (40−42%) for C800R, C1000R, and C1100R. A decrease of this contribution is observed for C1200R (28%) and C1300R (24%). For C1400R, there is no α-Fe contribution. A similar evolution is observed for γ-Fe-C. Fe_3C was detected in only four of the nanocomposites (C800R, C1000R, C1100R, and C1200R). The Fe_3C contribution is weak (<7%), and therefore, the corresponding hyperfine parameters had to be kept fixed in the fit procedures. For the sake of clarity, the evolution of the proportions of the iron species in hercynite, corundum, and the reduced phases (α-Fe, γ-Fe-C, and Fe_3C) versus the calcination temperature of the oxide catalytic material is presented in Figure 9a. It clearly appears that the content of the reduced forms of iron (α-Fe, γ-Fe, and Fe_3C) sharply diminishes when the calcination temperature is higher than 1100 °C, which is correlated with the increase of the proportion of the iron species in hercynite. Earlier studies have revealed that either no detectable amounts[4,8,9,16,19] or only a small amount (≤11%)[18] of hercynite are formed upon the H_2-CH_4 reduction when the catalytic material is an $Al_2O_3-Fe_2O_3$ solid solution (i.e., a Fe^{3+}/corundum phase). Therefore, the Fe^{2+} ions in hercynite detected in the present powders are mostly produced by the reduction of the Fe^{3+} ions that were present in mullite in the catalytic material. The total proportion of the reduced species is higher than the proportion of the Fe^{3+}/corundum in the starting material, which shows that a fraction of the reduced species is formed by the reduction of the Fe^{3+}/mullite, with or without the formation of intermediate Fe^{2+}/hercynite. However, the calculation of a reduction ratio from the respective proportions of, on

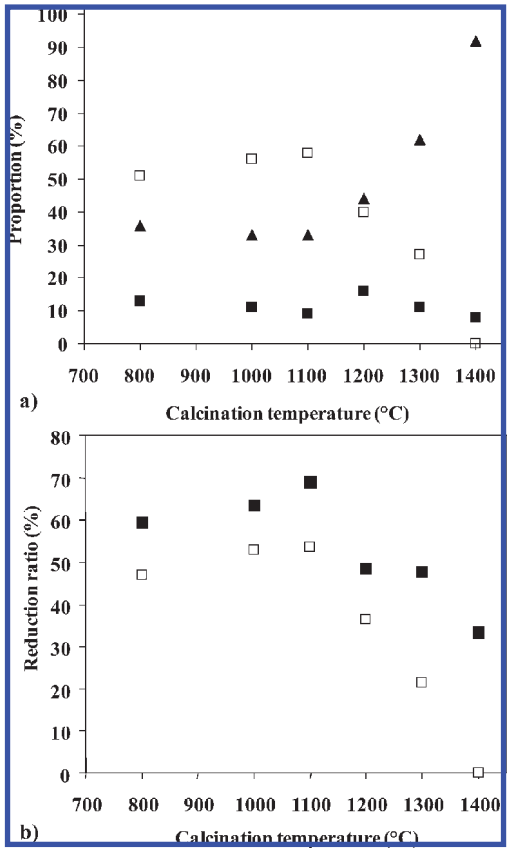

Figure 9. (a) Evolution of the proportions of the iron species in the reduced phases (α-Fe, γ-Fe-C, and Fe_3C) (open squares), corundum (solid squares), and hercynite (triangles) versus the calcination temperature of the catalytic material. (b) Reduction ratio for the corundum (solid squares) and mullite (open squares) phases; see text for details.

the one hand, Fe^{3+}/corundum in the starting material (Table 1) and in the nanocomposite powders (Table 2), and, on the other hand, of Fe^{3+}/mullite (Table 1) and Fe^{2+}/hercynite (Table 2), reveals that the reducibility of both phases is much hampered when the calcination temperature is higher than 1100 °C (Figure 9b).

4. Conclusions

Powders of iron-substituted mullite have been prepared by combustion and further calcination in air at different temperatures. A detailed study involving notably Mössbauer spectroscopy evidenced that the iron ions are distributed between the mullite phase and a corundum phase that progressively dissolves into mullite upon the increase in calcination temperature. Using these powders as catalytic materials has for the first time permitted preparation of carbon nanotube−Fe−mullite nanocomposites by a direct method involving a reduction in H_2-CH_4 and without any mechanical mixing step. The Fe^{3+} ions present in both the mullite and corundum phases are reduced to form metallic particles that are detected as α-Fe, Fe_3C, and γ-Fe-C. However, the major part of the Fe^{3+}/mullite ions are only partially reduced to Fe^{2+} ions in a hercynite ($FeAl_2O_4$) phase. The reducibility of the mullite and corundum phases is much hampered when the calcination temperature of the catalytic material is higher than 1100 °C. The carbon nanotubes formed by the catalytic decomposition of CH_4 on the smallest metal particles are mostly double-walled and multiwalled, although some carbon nanofibers are also observed.

Acknowledgment. This work was partially funded by the Fund for Scientific Research−Flanders and by the Special Research Fund (*BOF, Bijzonder Onderzoeksfonds*), UGent (B/06633), Belgium. X.H. thanks the governement of the P.R. China for a grant. The authors would like to thank Mr. Lucien Datas for assistance with electron microscopy observations, which were performed at TEMSCAN, the "Service Commun de Microscopie Electronique à Transmission", Université Paul Sabatier, Toulouse.

References and Notes

(1) Peigney, A.; Laurent, Ch. In *Ceramic Matrix Composites: Microstructure, Properties and Applications*; Low, I. M., Ed.; Woodhead Publishing Ltd: Cambridge, 2006; pp 309−333.

(2) Peigney, A.; Laurent, Ch.; Dobigeon, F.; Rousset, A. *J. Mater. Res.* **1997**, *13*, 613.

(3) Hafner, J. H.; Bronikowski, M. J.; Azamian, B. K.; Nikolaev, P.; Rinzler, A. G.; Colbert, D. T.; Smith, K. A.; Smalley, R. E. *Chem. Phys. Lett.* **1998**, *296*, 195.

(4) Peigney, A.; Coquay, P.; Flahaut, E.; Vandenberghe, R. E.; De Grave, E.; Laurent, Ch. *J. Phys. Chem. B* **2001**, *105*, 9699.

(5) Flahaut, E.; Govindaraj, A.; Peigney, A.; Laurent, Ch.; Rousset, A.; Rao, C. N. R. *Chem. Phys. Lett.* **1999**, *300*, 236.

(6) Flahaut, E.; Peigney, A.; Laurent, Ch.; Rousset, A. *J. Mater. Chem.* **2000**, *10*, 249.

(7) Garcia, F. L.; Peigney, A.; Laurent, Ch. *Mater. Res. Bull.* **2008**, *43*, 3088.

(8) Laurent, Ch.; Peigney, A.; Rousset, A. *J. Mater. Chem.* **1998**, *8*, 1263.

(9) Peigney, A.; Laurent, Ch.; Rousset, A. *J. Mater. Chem.* **1999**, *9*, 1167.

(10) Coquay, P.; De Grave, E.; Vandenberghe, R. E.; Dauwe, C; Flahaut, E.; Laurent, Ch.; Peigney, A.; Rousset, A. *Acta Mater.* **2000**, *48*, 3015.

(11) Coquay, P.; Vandenberghe, R. E.; De Grave, E.; Fonseca, A.; Piedigrosso, P.; Nagy, J. B. *J. Appl. Phys.* **2002**, *92*, 1.

(12) Coquay, P.; De Grave, E.; Peigney, A.; Vandenberghe, R. E.; Laurent, Ch. *J. Phys. Chem. B* **2002**, *106*, 13186.

(13) Coquay, P.; Peigney, A.; De Grave, E.; Vandenberghe, R. E.; Laurent, Ch. *J. Phys. Chem. B* **2002**, *106*, 13199.

(14) Coquay, P.; Peigney, A.; De Grave, E.; Flahaut, E.; Vandenberghe, R. E.; Laurent, Ch. *J. Phys. Chem. B* **2005**, *109*, 17813.

(15) Coquay, P.; Flahaut, E.; De Grave, E.; Peigney, A.; Vandenberghe, R. E.; Laurent, Ch. *J. Phys. Chem. B* **2005**, *109*, 17825.

(16) De Resende, V. G.; De Grave, E.; Peigney, A.; Laurent, Ch. *J. Phys. Chem. C* **2008**, *112*, 5756.

(17) De Resende, V. G.; Cordier, A.; De Grave, E.; Weibel, A.; Peigney, A.; da Costa, G. M.; Laurent, Ch.; Vandenberghe, R. E. *J. Mater. Res.* **2008**, *23*, 3096.

(18) De Resende, V. G.; De Grave, E.; Cordier, A.; Weibel, A.; Peigney, A.; Laurent, Ch. *Carbon* **2009**, *47*, 482.

(19) Cordier, A.; de Resende, V. G.; De Grave, E.; Peigney, A.; Laurent, Ch. *J. Phys. Chem. C* **2008**, *112*, 18825.

(20) Reshetenko, T. V.; Avdeeva, L. B.; Ushakov, V. A.; Moroz, E. M.; Shmakov, A. N.; Kriventsov, V. V.; Kochubey, D. I.; Pavlyukhin, Y. T.; Chuvilin, A. L.; Ismagilov, Z. R. *Appl. Catal., A: Gen.* **2004**, *270*, 87.

(21) Kónya, Z.; Vesselényi, I.; Lázár, K.; Kiss, J.; Kiricsi, I. *IEEE Trans. Nanotechnol.* **2004**, *3*, 73.

(22) Bakandritsos, A.; Simopoulos, A.; Petridis, D. *Chem. Mater.* **2005**, *17*, 3468.

(23) Pérez-Cabero, M.; Taboada, J. B.; Guerrero-Ruiz, A.; Overweg, A. R.; Rodríguez-Ramos, I. *Phys. Chem. Chem. Phys.* **2006**, *8*, 1230.

(24) Chen, J.; Kuno, A.; Matsuo, M.; Tsukada, T.; Tamura, T.; Osato, K.; Shan, J. Y.; Munekane, F.; Kim, Y. A.; Hayashi, T.; Endo, M. *Carbon* **2008**, *46*, 391.

(25) Agrell, O.; Smith, J. V. *J. Am. Ceram. Soc.* **1960**, *43*, 69.

(26) Ossaka, J. *Nature* **1961**, *191*, 1000.

(27) Aramaki, S.; Roy, R. *J. Am. Ceram. Soc.* **1962**, *45*, 229.

(28) Sadanaga, R.; Tokonami, M.; Takeuchi, Y. *Acta Crystallogr.* **1962**, *15*, 65.

(29) Aksay, I. A.; Pask, J. A. *J. Am. Ceram. Soc.* **1975**, *58*, 507.

(30) Cameron, W. E. *Am. Mineral.* **1977**, *62*, 747.

(31) Wang, J.; Kou, H.; Liu, X.; Pan, Y.; Guo, J. *Ceram. Int.* **2007**, *33*, 719.

(32) Chandran, R. G.; Patil, K. C. *Mater. Lett.* **1990**, *10*, 291.

(33) Chandran, R. G.; Chandrashekar, B. K.; Ganguly, C.; Patil, K. C. *J. Eur. Ceram. Soc.* **1996**, *16*, 843.

(34) Burgos-Montes, O.; Moreno, R.; Colomer, M.; Farinas, J. *J. Am. Ceram. Soc.* **2006**, *89*, 484.

(35) Patil, K. C. *Bull. Mater. Sci.* **1993**, *16*, 533.

(36) Cameron, W. E. *Phys. Chem. Miner.* **1977**, *1*, 265.

(37) Schneider, H. *Ceram. Trans.* **1990**, *6*, 135.

(38) Cardile, C. M.; Brown, I. W. M.; Mackenzie, K. J. D. *J. Mater. Sci. Lett.* **1987**, *6*, 357.

(39) Parmentier, J.; Vilminot, S.; Dormann, J.-L. *Solid State Sci.* **1999**, *1*, 257.

(40) Mack, D. E.; Becker, K. D.; Schneider, H. *Am. Mineral.* **2005**, *90*, 1078.

(41) Cordier, A.; Peigney, A.; De Grave, E.; Flahaut, E.; Laurent, Ch. *J. Eur. Ceram. Soc.* **2006**, *26*, 3099.

(42) Menil, F. *J. Phys. Chem. Solids* **1985**, *46*, 763.

(43) Larsson, L.; O'Neill, H. St. C.; Annersten, H. *Eur. J. Mineral.* **1994**, *6*, 39.

JP901780F